"Glacial cooling and climate sensitivity revisited"

Jessica E. Tierney[1*], Jiang Zhu[2], Jonathan King[1], Steven B. Malevich[1], Gregory J. Hakim[3], & Christopher J. Poulsen[2]

[1] Department of Geosciences, University of Arizona, Tucson, AZ 85721, USA
[2]Department of Earth and Environmental Sciences, University of Michigan, Ann Arbor MI 48109, USA
[3]Department of Atmospheric Sciences, University of Washington, Seattle, WA 98195, USA
*corresponding author: jesst@arizona.edu

This is a non-peer reviewed preprint submitted to EarthArXiV.
This paper has been submitted to *Nature*.

Glacial cooling and climate sensitivity revisited

Jessica E. Tierney[1*], Jiang Zhu[2], Jonathan King[1], Steven B. Malevich[1], Gregory J. Hakim[3], Christopher J. Poulsen[2]

[1]Department of Geosciences, The University of Arizona, Tucson, AZ 85721, USA

[2]Department of Earth and Environmental Sciences, University of Michigan, Ann Arbor, MI 48109, USA

[3]Department of Atmospheric Sciences, University of Washington, Seattle, WA 98195, USA

[*]To whom correspondence should be addressed; e-mail: jesst@arizona.edu.

The Last Glacial Maximum (LGM), one of the best-studied paleoclimatic intervals, offers a prime opportunity to investigate how the climate system responds to changes in greenhouse gases (GHGs) and the cryosphere. Previous work has sought to constrain the magnitude and pattern of glacial cooling from paleothermometers, but the uneven distribution of the proxies, as well as their uncertainties, has challenged the construction of a full-field view of the LGM climate state. Here, we combine a large collection of geochemical proxies for sea-surface temperature with an isotope-enabled climate model ensemble to produce a field reconstruction of LGM temperatures using data assimilation. The reconstruction is validated with withheld proxies as well as independent ice core and speleothem δ^{18}O measurements. Our assimilated product provides a precise constraint on global mean LGM cooling of −5.9°C (−6.3 – −5.6°C, 95% CI). Given assumptions concerning the radiative forcing of GHGs, ice sheets, and aerosols, this cooling translates to an equilibrium climate sensitivity (ECS) of 3.2°C (2.2 – 4.3°C, 95% CI), a value that is higher than previous estimates and but consistent with the traditional consensus range of 2 – 4.5°C.

Paleoclimatologists have long sought to refine our view of temperature changes during the LGM, as both a benchmark for climate models and a constraint on Earth's climate sensitivity. In the 1970s, the Climate Long-Range Investigation, Mapping and Prediction (CLIMAP) project collated assemblages of foraminifera, radiolarians, and coccolithophores and used transfer functions to create maps of seasonal sea-surface temperatures (SSTs) for the LGM [1]. Along with geological constraints on sea level and ice sheet extents, these maps were used as boundary conditions for pioneering atmospheric Global Climate Model (GCM) simulations—the first Paleoclimate Modeling Intercomparison Project (PMIP) [2]. Three decades later, the Multiproxy Approach for the Reconstruction of the Glacial Ocean Surface (MARGO) project remapped the LGM oceans using foraminiferal, radiolarian, diatom, and dinoflagellate transfer functions and two geochemical proxies—the unsaturation index of alkenones ($U_{37}^{K'}$) and the Mg/Ca ratio of planktic foraminifera [3]. This product has served as a touchstone for model-data comparison in PMIP2 and 3 [4] as well as calculations of climate sensitivity [5].

In spite of this extensive work, estimates of global cooling during the LGM remain poorly constrained due to proxy uncertainties and methodological limitations. Microfossils occasionally present "no-analogue" assemblages; i.e. groups of species that are not observed today and therefore are difficult to interpret. In the LGM in particular, no-analogue assemblages appear in North Atlantic dinocysts [1] and tropical Pacific foraminifera [6], and have cast doubt upon the CLIMAP and MARGO inference of relatively mild LGM cooling in the tropics and subtropics [7–9]. Likewise, geochemical proxies are subject to seasonal biases and sensitivity to non-thermal controls, all of which affect calculated SSTs [10,11]. Beyond proxy uncertainties, the data from the LGM present a methodological challenge in that they are not evenly distributed in space; the data cluster near coasts, where there are sufficient sediment accumulation rates. This complicates the calculation of both regionally- and globallyaveraged values. Furthermore, the translation of changes in SST to global mean surface air temperature (GMST)—the quantity needed for calculations of climate sensitivity—requires the use of an uncertain scaling factor [12]. Thus, estimates of the change in LGM GMST (ΔGMST) range from $-1.7°C$ to $-8.0°C$ [5,12–18], and translate to poorly bounded estimates of climate sensitivity of 1–6°C per doubling of CO_2 [19].

Here, we infer the magnitude and spatial pattern of LGM cooling using geochemical SST proxies, Bayesian calibration models, isotope-enabled climate model simulations, and offline data assimilation. Specifically, SST proxy observations are assimilated using Bayesian proxy system models and new simulations conducted with the isotope-enabled Community Earth System Model (iCESM)[20]. The resulting estimates of GMST change are combined with published constraints on radiative forcing to produce new probabilistic estimates of climate sensitivity based on the LGM climate state.

Our data collection consists of 955 LGM (19–23 ka) and 880 late Holocene (0–4 ka) data points (Fig. 1, see Methods). For the purposes of this study, the Late Holocene average is interpreted as representative of the preindustrial (PI) climate state, and is the benchmark against which we compute LGM cooling (see Methods). Distinct from previous work, this study focuses exclusively on geochemical proxies for SST; specifically, $U_{37}^{K'}$, TEX_{86}, $\delta^{18}O$, and Mg/Ca. We have developed Bayesian calibration models for all of these proxy systems [10,11,21,22], which enables us to propagate calibration uncertainty as well as use forward models for data assimilation. While including assemblage data would improve spatial coverage, the outstanding no-analogue problems and lack of comparable Bayesian models prevent us from using these data in the framework presented here.

In order to circumvent problems associated with the spatial representation and averaging, we use an offline data assimilation technique [23] (see Methods) to blend information from proxies with full-field dynamical constraints from iCESM. The assimilation begins with an ensemble "prior" of possible climate states taken from the model; in our case, these are 50-yr average states from simulations of the glacial state (18 and 21 ka) and the late Holocene (PI and 3 ka) (see Methods). The water-isotope-enabled model simulations facilitate the direct assimilation of δ^{18}O data (comprising 60% of our collection; Fig. 1), without the need to rely on empirical relationships between seawater δ^{18}O and salinity derived from present-day observations. At locations where there are proxy data, values from the ensemble prior are translated into proxy units using our Bayesian forward models in order to calculate the "innovation"—the difference between the observed proxy value and computed value from the model ensemble. The innovation is weighted by the Kalman gain, which considers both the covariance of proxy with the rest of the climate fields as well as the uncertainties in both the proxy observation and the model ensemble. This value is then added to the prior ensemble to produce a ensemble posterior climate state (see Methods for a mathematical description). For each time interval (LGM and Late Holocene) we conducted 25 assimilation experiments with a 40-member model ensemble in which we withheld 25% of the proxy data at random in order to calculate verification statistics (see Methods). These collectively yield a total of 1000 ensemble realizations of LGM and late Holocene climate.

The assimilated posterior SST field shows distinctive spatial patterns in LGM cooling (Fig. 2a), with changes in SST in excess of $-8°$C in the north Atlantic, north Pacific, and the Pacific sector of the Southern Ocean; enhanced cooling in eastern boundary upwelling zones; and reduced cooling in the western boundary regions. Many of these features are broadly consistent with CLIMAP and MARGO; however an important difference is that we do not observe warming in the subtropical gyres, a feature that is associated with assemblage data [1,3] (Fig. 2a). In the Indian Ocean, our reconstructed cooling pattern closely resembles the proxies and reflects the impact of the exposed Sunda and Sahul shelves [24]. Previous investigations of cooling in the glacial tropical Pacific offer conflicting conclusions; some suggest enhanced cooling in the eastern equatorial Pacific (EEP; as we observe here) [6], while others suggest greater cooling in the warm pool [25]. Analysis of our proxy collection (separate from the assimilated product) indicates that there is no significant difference in the magnitude of cooling between the warm pool and EEP (-0.2 ± 1.0 °C, 2σ, see Methods). This could reflect a limitation of the proxy network, which is biased towards the coasts (Fig. 1). The stronger cooling in the EEP in the assimilated posterior thus reflects the CESM prior, and possibly the influence of proxies that are teleconnected to EEP, such as those situated along the California margin.

The covariance of SST with surface air temperature (SAT) allows us to recover a posterior ensemble for the latter directly from the assimilation algorithm, rather than having to scale from one to the other [12]. Over land, we observe the expected large cooling over the Northern Hemisphere ice sheets, but noticeably little cooling in Alaska and western Beringia (Fig. 2c). These results agree with long-standing observations that these locations remained unglaciated during the LGM [26] and experienced minimal cooling or even a slight warming [27], likely due to dynamical changes induced by the Laurentide Ice Sheet [28,29].

Our reconstruction provides updated estimates of tropical cooling. The glacial change in SAT across the tropics (30°S – 30°N) is −3.9 (−4.2 – −3.7°C, 95% CI). This estimate is greater than the PMIP2 and 3 multi-model range of −1.6 – −3.2°C[30], but is not as large as calculations based on snowlines of tropical glaciers [31] and noble gases [32] (ca. −5°C). Our reconstruction indicates that tropical SSTs cooled by 3.5°C (3.7 – 3.3°C, 95% CI). This value is larger than the spatial mean computed from the tropical SST proxies on their own (−2.5°C, −2.8 – −2.2°C, 95% CI), partly due to the enhanced cooling throughout the east-central tropical Pacific in the assimilated posterior (Fig. 2a). However, the magnitude of both the proxy- and data assimilation-inferred tropical SST cooling is far greater than CLIMAP or MARGO estimates (-0.8°C and -1.5°C, respectively) and closer to the estimate of refs. [8] (-2.7°C) and [33] (-2.8°C).

To assess the reliability of our reconstruction, we included the δ^{18}O of precipitation ($\delta^{18}O_p$) in our model prior so we could compare the posterior ensemble of this variable to independent ice core and speleothem proxy data (see Methods). Overall, our reconstruction explains 65% of the variance in observed $\Delta\delta^{18}O_p$ (Fig. 3a). This is a marked improvement over the prior, which only explains 35% of the variance (Extended Data Figure 1). A notable feature captured by our reconstruction is the difference in $\Delta\delta^{18}O_p$ between ice core sites in west and east Antarctica (Fig. 3b); the latter region is warmer (Fig. 2b) and experiences less isotopic depletion. At face value, a warmer east Antarctica contradicts previous work; at Epica Dome C, ice core δ^{18}O is interpreted to indicate a change in SAT of ~ -8°C [34], while our assimilated product indicates a more modest cooling of -5°C. However, the former estimate assumes that the δ^{18}O-SAT relationship remains constant in time [34]. Isotope-enabled modeling experiments have shown that the δ^{18}O-SAT slope in Antarctica may have been different during the LGM, and moreover strongly depends on changes in Southern Ocean SSTs [35]. The relatively smaller cooling over the Indian Ocean sector of the Southern Ocean in our reconstruction results in a steeper slope and explains why we are able to reproduce the magnitude of $\delta^{18}O_p$ response with warmer temperatures.

The fact that our reconstruction can match independent $\delta^{18}O_p$ proxies suggests that it provides a reasonable estimate of global LGM climate. Since the data assimilation technique provides us with full fields, we can compute values of both global SST (GSST) and mean surface temperature (GMST) change during the LGM without needing to consider missing values or use a scaling factor [12]. Our calculated change in GSST is -3.2°C (-3.4 – -2.9°C, 95% CI) (Fig. 2b). This is much more tightly constrained than the model prior, which spans −2.7 – −4°C (Fig. 2b), reflecting the influence of the data. The assimilated ΔGSST is slightly larger than the proxy data suggest (−2.8°C, −3.0 – −2.7°C, 95% CI, Fig. 2b); however as emphasized, data-only estimates are biased by the fact that the field is sampled incompletely and unevenly. The ΔGSST from data assimilation agrees well with estimates of glacial cooling based on a subset of SST proxies spanning multiple glacial-interglacial cycles (−3.1°C) [18], but is much larger than CLIMAP (−1.2°C) and MARGO (−1.9°C).

The change in GMST in the assimilated product is −5.9°C (−6.3 – −5.6°C, 95% CI). As with ΔGSST, this result falls on the lower end of a proxy-only estimate and the upper end of the model prior (Fig. 2d). A ΔGMST of ca. −6°C agrees with a number of previous studies, including those that estimated LGM cooling from a restricted network of proxies spanning multiple glacial/interglacial cycles [12,18], noble gas measurements in ice cores [17], and changes in tropical SSTs [13,14] (Fig. 4a). However, our calculated ΔGMST does not overlap with the estimates that utilized the MARGO product [5,16] (−2 – −4°C), or an average of time-continuous marine and terrestrial temperature proxies [15] (Fig. 4a). Our ΔGMST estimate falls on the lower end of the PMIP2 and 3 model range (−3.1 – −5.9°C) [19].

Our assimilated estimate of ΔGMST supports an emerging consensus that LGM cooling is larger than previously assumed (Fig. 4a). Since it is based on a full-field reconstruction, our ensemble ΔGMST value is narrower than previous work and thus can be used to provide tighter constraints on ECS. To calculate an ECS that approximates the classical "Charney" definition, we must consider, in addition to greenhouse gas forcing (ΔR_{GHG}) the slow feedback processes that affect LGM climate, which following ref. [36] are treated here as radiative forcings. These include albedo changes associated with the expanded land ice and lowered sea level (ΔR_{ICE}) and increases in mineral dust aerosols (ΔR_{AE}). While vegetation changes could also impact LGM climate, we do not consider these here because biome reconstructions are poorly defined outside of the northern high latitudes [37], challenging determination of a global ΔR [38].

We estimate ΔR_{GHG}, ΔR_{ICE}, and ΔR_{AE} from published values in the literature and propagate uncertainties associated with these into the calculations of ECS (see Methods). We show results with and without aerosol forcing (ΔR_{AE}) for comparison with previous work (Fig. 4b). Without aerosols, ECS is 3.5°C (2.6 – 4.5 °C, 95% CI); with aerosols, ECS is 3.2°C (2.2 – 4.3 °C, 95% CI). With our ΔGMST from data assimilation, global temperature change is no longer the primary source of uncertainty; it accounts for about 20% of the 95% CI in each estimate (Fig. 4b). Rather, most of the uncertainty comes from the forcings (Fig. 4b). ΔR_{GHG} can be directly estimated from ice core GHG concentrations and simplified equations (-2.81 W/m^2) but still carries a 10% (90% CI) uncertainty. There is an additional 10% uncertainty associated with the doubling of CO_2 (3.80 W/m^2) [39] such that GHG forcing altogether accounts for $\sim$ 25% of the 95% CI. ΔR_{ICE} is estimated from CESM and available PMIP2 and 3 simulations (see Methods) and its value varies between -2.6 and -5.2 W/m^2, thus accounting for $\sim$ 35% of the uncertainty in ECS. Finally, while it is well-known that the LGM atmosphere was dustier [40] the magnitude of ΔR_{AE} also varies widely across models (ca. 0 – -2 W/m^2) [40] and contributes $\sim$ 20% of the 95% CI.

Recently, it has been argued that ice sheets are not as "effective" as greenhouse gases in terms of global radiative forcing, because their impact might be concentrated at high latitudes [41,42]. We explore this possibility by presenting a distribution of ECS with an ice sheet efficacy (ε) of 0.65 (see Methods) (Fig. 4b). Under this scenario, the median ECS rises to 3.9 with a 95% CI of 2.7 to 5.2.

Even though uncertainties in the radiative forcings yield broad distributions, we can use these new calculations to make probabilistic statements concerning ECS. Given the uncertainty space explored here, the LGM data suggest ECS is virtually certain (>99% probability) to be above 2.1°C and below 5.4°C, with the latter only plausible under a condition of low ice sheet efficacy. Assuming ice efficacy of 1, ECS is very likely (90% probability) between 2.3°C and 4.1°C. These are substantially tighter constraints on ECS than those stated in the Intergovernmental Panel on Climate Change (IPCC) AR5 report (1–6°C per doubling of CO_2)[19] and arise mainly from our precise estimate of ΔGMST from data assimilation.

ECS calculated here is in excellent agreement with the traditional consensus range of 2–4.5 °C [43,44]. Unlike previous work, we find little evidence that ECS based on the LGM climate is abnormally low [5,38]. ECS is unlikely to remain constant across climate states; rather, paleoclimate and modeling evidence suggest that it scales with background temperature, with lower values during cold climates and higher values during warm states [45,46]. Taking this into consideration, our LGM results place a strong constraint on minimum ECS in the climate system, which is almost certainly greater than 2°C, and more likely between 3–4°C.

Methods

SST proxy data collection. We compiled a total of 955 and 880 proxy data points from the LGM and late Holocene (LH) time periods, respectively. Following MARGO, the LGM was defined as 19–23 ka [3]. The LH was defined as 0–4 ka to match the interval of time averaged for the LGM. This choice is consistent with previous LGM–LH comparisons [10,47]. For the purposes of this study, the LH is considered representative of preindustrial conditions. Although climate has certainly changed within the past 4,000 years in response to shorter-term forcings such as volcanic eruptions and solar irradiance, we posit that this assumption is reasonable in the context of the large, slow climate changes associated with orbitally-driven glacial–interglacial cycles. This differs from CLIMAP and MARGO, in which LGM cooling was calculated relative to 20^{th} century observations [1,3]. However, historical observations carry their own distinctive type of uncertainties [48] and also include the signature of anthropogenic global warming, so are not ideal in terms of isolating the LGM climatic response. Furthermore, using proxy estimates of the preindustrial climate, rather than observational estimates, offers an "apples-to-apples" comparison with the LGM.

The proxy data consist of both continuous time series that pass through the LGM and the LH, as well as data from "timeslice" studies that focused on the average LGM climate state. The latter derive in part from the MARGO collection, with additional data from more recent studies. In many cases, LGM slice data were not accompanied by corresponding LH data. To provide matching data for these cases, we searched the core top datasets for each proxy system for a nearby value, with a cutoff radius of 1000 km. This provided roughly similar spatial coverage between the LGM and LH target slices (Fig. 1). Core tops that were used as LH data were subsequently removed from the calibration datasets, and the parameters for the Bayesian calibration models were recalculated without these data, so as to avoid circularity. However, since the number of core tops used in the data synthesis is small (ca. 100 or less) relative to the size of the core top datasets (ca. 1000) the affect on the model parameters was negligible.

The time series consist of 261 core sites with radiocarbon-based age models. Prior to taking time-averages from these proxy data we recalibrated all age models using the Marine13 radiocarbon curve and the BACON age modeling software (translated into Python as `snakebacon` and available here: `https://github.com/brews/snakebacon`) to ensure consistent treatment. Not all of the core sites extend through the LGM and/or the LH, so not all of these sites are represented in the analysis. However, many of these sites typically contain more than one proxy for SST, thus the total number of data constraints from the time series data is 334 for the LGM, and 275 for the LH.

Model Simulations. We employ the water isotope-enabled Community Earth System Model (iCESM) [20], which is based on CESM version 1.2 [49]. iCESM has the capability to explicitly simulate the transport and transformation of water isotopes in hydrological processes in the atmosphere, land, ocean, and sea ice [20]. iCESM can accurately reproduce instrumental records of both the physical climate and the water isotopes [20,49].

We conducted iCESM1.2 simulations of the Late Holocene and the LGM, consisting of timeslices of PI, 3, 18, and 21 ka. PI used standard climatic forcings at A.D. 1850. Slice simulations of 3, 18, and 21 ka used boundary conditions of GHGs, Earth orbits, and ice sheets following the PMIP4 protocol [50]. Specifically, CO_2, CH_4, and N_2O concentrations were 275 ppm, 580 ppb, and 270 ppb for 3 ka, 190 ppm, 370 ppb, and 245 ppb for 18 ka, and 190 ppm, 375 ppb, and 200 ppb for 21 ka. Changes in surface elevation, albedo, and land ocean distribution associated to ice sheets were derived from the ICE-6G reconstruction [51]. The Late Holocene time slices (PI and 3 ka) and the LGM slices (21 and 18 ka) were extended from previous iCESM1.2 simulations [52], which have reached quasi-equilibrium in both the physical climate and the water isotopes. Ice-volume effects on the seawater isotopic composition have been considered in the 18- and 21-ka simulations, which have a global volume mean of 1.05‰, compared to the value of 0.05‰ in the PI and 3-ka simulations. All the timeslice simulations were run for 900 years with a horizontal resolution of 1.9° × 2.5° (latitude × longitude) for the atmosphere and land, and a nominal 1 degree displaced pole Greenland grid for the ocean and sea ice.

We also made use of available iCESM1.3 simulations of the LGM and PI [52]. iCESM1.3 differs from iCESM1.2 primarily in the gravity wave scheme, along with a few bug fixes in the cloud microphysics and radiation [53]. The iCESM1.3 preindustrial and LGM simulations have a length of 400 and 1000 years, respectively.

Data Assimilation. The data assimilation technique uses the offline ensemble Kalman filter method developed for the Last Millennium Reanalysis [23,54], which solves the following update equation to compute an ensemble of posterior climate states ($\boldsymbol{X}_{posterior}$):

$$\boldsymbol{X}_{posterior} = \boldsymbol{X}_{prior} + \mathbf{K}(\boldsymbol{y} - \boldsymbol{Y_e}) \tag{1}$$

$\boldsymbol{X}_{prior}$ is a prior ensemble of climate states taken from iCESM. In a typical data assimilation application, the length of time represented by the ensemble would equal the length of time represented by the data; e.g. annual data would be used to update an annual prior. However, in our case the data represent average conditions across 4,000 years. Since we cannot run iCESM for 100,000+ years, we must use a different time average for our model prior. Experimentation with time-averaging the model states revealed that once the average exceeded the interannual time scale, the patterns in the covariance structures were insensitive to the length of the average (e.g., 10-year averages looked similar to 50-year averages). Thus we chose 50 years – the longest time average that we could use while still retaining enough ensemble members for the assimilation technique (40 members).

$\boldsymbol{y}-\boldsymbol{Y_e}$ is the innovation – the difference between the vector of observed proxy values ($\boldsymbol{y}$) and the matrix of proxy values calculated from the model prior ($\boldsymbol{Y_e}$) at the same locations. This calculation takes place in proxy units – model output is translated into proxy values using our Bayesian forward models [10,11,21,22]. For $U^{K'}_{37}$ and TEX_{86}, the forward models require only SSTs (monthly for $U^{K'}_{37}$, to account for seasonal responses in the North Atlantic, North Pacific, and Mediterranean regions [10]; annual for TEX_{86}). The model for $\delta^{18}O$ of planktic foraminifera ($\delta^{18}O_c$) requires monthly SST and the annual $\delta^{18}O$ composition of seawater [22]. $\delta^{18}O_c$ is computed for the optimal growing season using the species-specific hierarchical model described in ref. [22]. The model for Mg/Ca of planktic foraminifera requires monthly SST and sea-surface salinity (SSS), as well as surface water pH, bottom water calcite saturation state (Ω), and the cleaning method used in the laboratory [11]. The latter was recorded as part of the data collection effort, but for pH and Ω we must make assumptions, since iCESM does not simulate the ocean carbonate system. In the absence of good information regarding spatial changes in Ω, we assume that it is the same as today for each given site location, with values drawn from GLODAPv2 [55]. For pH, we use modern estimates from GLODAPv2 for the LH timeslice, and then for the LGM we add 0.13 units to the modern values to account for the global increase in pH due to lowered CO_2, following refs. [11,56]. As with $\delta^{18}O_c$, Mg/Ca is forward-modeled for the optimal growing season using the species-specific hierarchical model described in ref. [11]. In this manner, the seasonal preferences of foraminifera are explicitly accounted for in the assimilation.

$\mathbf{K}$ is the Kalman gain, which weights the innovation according to the covariance of the forward-modeled proxy value with the rest of the climate state (the numerator), as well as the uncertainty of the model ensemble and the proxy observation (the denominator). Following ref. [57], $\mathbf{K}$ is defined as:

$$\mathbf{K} = \frac{\boldsymbol{W}_{loc} \circ \left[\boldsymbol{X}'_{prior} \boldsymbol{Y}_{\boldsymbol{e}}'^{\top}/(n-1)\right]}{\boldsymbol{Y}_{loc} \circ \left[\boldsymbol{Y}'_{\boldsymbol{e}} \boldsymbol{Y}_{\boldsymbol{e}}'^{\top}/(n-1)\right] + \boldsymbol{R}} \tag{2}$$

where $\boldsymbol{X}'_{prior}$ and $\boldsymbol{Y}'_{\boldsymbol{e}}$ are the matrices of deviations, e.g. $\boldsymbol{X}'_{prior} = \boldsymbol{X}_{prior} - \overline{\boldsymbol{X}}_{prior}$, $\boldsymbol{R}$ is a diagonal matrix of the uncertainty (as a variance) of each proxy observation, and $\boldsymbol{W}_{loc}$ and $\boldsymbol{Y}_{loc}$ are weights that apply a covariance localization, a distance-weighted filter that limits the influence of each proxy in space [58]. n is the number of ensemble members, and division by $(n-1)$ is applied to obtain an unbiased estimate. $\circ$ denotes element-wise multiplication.

Following ref. [57], the update equation (Eq. 1) is solved by decomposing the problem into an update of the mean value of the prior state ($\overline{\boldsymbol{X}}_{prior}$) and the deviations from the mean ($\boldsymbol{X}'_{prior}$):

$$\overline{\boldsymbol{X}}_{posterior} = \overline{\boldsymbol{X}}_{prior} + \mathbf{K}(\boldsymbol{y} - \overline{\boldsymbol{Y}}_{e}) \tag{3}$$

$$\boldsymbol{X}'_{posterior} = \boldsymbol{X}'_{prior} - \tilde{\mathbf{K}} \boldsymbol{Y}'_{\boldsymbol{e}} \tag{4}$$

where $\tilde{\mathbf{K}}$ is defined as:

$$\tilde{\mathbf{K}} = \boldsymbol{W}_{loc} \circ \left[\boldsymbol{X}'_{prior} \boldsymbol{Y}_{\boldsymbol{e}}'^{\top}/(n-1)\right] \left[\left(\sqrt{\boldsymbol{Y}_{loc} \circ \left[\boldsymbol{Y}'_{\boldsymbol{e}} \boldsymbol{Y}_{\boldsymbol{e}}'^{\top}/(n-1)\right] + \boldsymbol{R}}\right)^{-1}\right]^{\top} \times \left[\sqrt{\boldsymbol{Y}_{loc} \circ \left[\boldsymbol{Y}'_{\boldsymbol{e}} \boldsymbol{Y}_{\boldsymbol{e}}'^{\top}/(n-1)\right] + \boldsymbol{R}} + \sqrt{\boldsymbol{R}}\right]^{-1} \tag{5}$$

The full posterior ensemble is then recovered through:

$$\boldsymbol{X}_{posterior} = \overline{\boldsymbol{X}}_{posterior} + \boldsymbol{X}'_{posterior} \tag{6}$$

$\boldsymbol{R}$ and the covariance localization weights ($\boldsymbol{W}_{loc}$, $\boldsymbol{Y}_{loc}$) are user-defined, so we used validation metrics based on withheld SST proxies and independent proxies for the oxygen isotopic composition of precipitation ($\delta^{18}O_p$) to guide our choices. The most conservative values for $\boldsymbol{R}$ are the σ^2 terms given by the global Bayesian regression models for each proxy – we denote this as $\boldsymbol{R}_g$. In temperature space, these translate to 1.5–4°C 1σ errors. However, because these integrate uncertainties for locations across the entire world, they are likely too high for an individual proxy location (otherwise, one would expect that the proxies would not be able to detect LGM cooling at all). Rather, at a single site, proxy uncertainty is expected to lie somewhere between analytical precision and the global error. Unfortunately, this can only be directly observed by analyzing parallel sediment cores, which is not commonly done in paleoceanography. Thus, to experimentally determine an optimal value of $\boldsymbol{R}$, we systematically reduced it from $\boldsymbol{R}_g$ to $\boldsymbol{R}_g/100$ and analyzed validation statistics. For each of these experiments, the same 75% of the proxy data were used for the assimilation and the same 25% were withheld for validation. Values of SST, SSS, and $\delta^{18}O$ of seawater from the posterior ensemble were then forward-modeled to predict the withheld proxy values. We calculate both the coefficient of efficacy (CE) [59] and the root mean square error (RMSE) between the observed and mean of the predicted proxy values. These were calculated in normalized units in order to account for the different ranges of absolute proxy values between $U_{37}^{K'}$, TEX_{86}, $\delta^{18}O$, and Mg/Ca.

In addition, we calculated the R^2 between observed $\Delta\delta^{18}O_p$ (LGM $-$ PI) derived from ice cores and speleothems and predicted $\Delta\delta^{18}O_p$ from the assimilation. Ice core $\Delta\delta^{18}O_p$ were taken from the compilation in ref. [60] (their Table 1). Speleothem $\Delta\delta^{18}O_p$ values were computed from the SISAL database, version 1b [61]. We first searched the SISAL database for sites that contained both Late Holocene (0.2–4 ka, to exclude anthropogenically-influenced values) and LGM (19–23 ka) data and recorded the mean $\delta^{18}O$ of calcite or aragonite. We then converted these average δ^{18}O values to dripwater δ^{18}O (considered analogous to $\delta^{18}O_p$) following the recommendations of ref. [62] (their Eqs. 1–3). This conversion accounts for the influence of temperature on fractionation as well as kinetic effects, and converts from the VPDB to the VSMOW scale. These calculations require an estimate of cave temperature; for this we use the posterior SAT value from our data assimilation at the grid cells closest to the speleothem locations.

Extended Data Table 1 shows the validation results from scaling $\boldsymbol{R}_g$. For both the LGM and the Late Holocene, validation CE and RMSE are relatively insensitive to the choice of $\boldsymbol{R}$, although there is slight improvement up to $\boldsymbol{R}_g/10$. This is in part because the validation is being calculated across the globe and the spatial variation in proxy values is always large; indeed, even the prior produces decent prediction of the withheld proxies, particularly for the Late Holocene (Extended Data Table 1). More useful information can be gleaned from the comparison with the independent $\delta^{18}O_p$ data. Here, we observe a large increase in R^2 from the case of $\boldsymbol{R}_g$ to $\boldsymbol{R}_g/10$, from 0.42 (only slightly better than the prior, which is 0.37) to 0.66. This suggests that an increase in proxy precision drives the posterior closer to a state that agrees with the $\delta^{18}O_p$ proxies. However, it is also clear that if the proxy uncertainty is set too low ($\boldsymbol{R}_g/100$), the R^2 drops back down (0.44). Thus, there appears to be an ideal value of $\boldsymbol{R}$ somewhere near $\boldsymbol{R}_g/10$. This value of $\boldsymbol{R}$ translates to $\sim$ 0.5–1°C of 1σ uncertainty, depending on the proxy. This is greater than analytical error ($\sim 0.3\ 1\sigma$) and strikes us as a reasonable estimate of site-specific error.

Covariance localization is applied to minimize spurious relationships from producing artifacts at large distances away from the proxy location. Following ref. [23], we use the Gaspari-Cohn fifth-order polynomial [63] with a specified cut-off radius. To find an optimal radius, we experimented with values from ∞ (e.g. no localization) to 6,000 km and analyzed the same validation statistics as above. Extended Data Table 2 shows the results. As was the case with varying $\boldsymbol{R}$, validation CE and RMSE are not very sensitive to localization although they do improve up to a value of 12,000 km. The comparison with $\delta^{18}O_p$ shows that the best skill is achieved with a cut-off radius between 18,000–9,000 km. We thus use a value of 12,000 km.

Each time interval (LGM and LH) is carried out as a separate ensemble assimilation consisting of 25 iterations, in which we withhold 25% of the proxies at random for validation. Across all iterations, the validation CE is 0.95 for the LH and 0.92 for the LGM; the validation RMSE is 0.22 for the LH and 0.29 for the LGM (in normalized proxy units). Figure 3 in the main text shows the independent validation with the $\delta^{18}O_p$ proxies. The relatively good fit ($R^2 = 0.65$) is a substantial improvement over the model prior (Extended Data Figure 1).

Proxy-only estimates of LGM cooling. To provide a point of comparison for the results from data assimilation, we computed global and tropical ΔSST and ΔGMST from the proxy data in isolation. The proxy data were calibrated to SST using a our suite of Bayesian prediction models [10,11,21,22] producing 1000-member ensemble estimates for each data point. To approximate the proxy observational uncertainty ($\boldsymbol{R}$) used in the data assimilation (see discussion above), data were sorted along the ensemble dimension and normally-distributed site-level error ($\mathcal{N}(0,0.5)$°C) was added back to the ensemble. Global mean sea-surface temperature (GSST) was computed following the method of [46]—data were first binned and averaged into latitudinal bands, then latitudinal averages were used to calculate an area-weighted global average. Since the results are sensitive to the size of the bin [46] we computed an ensemble of GSST across bin sizes of 2.5° to 15° (at 2.5° intervals). GSST was scaled to global mean surface temperature (GMST) using the method of ref. [12], in which scaling factors (determined from PMIP LGM simulations) were drawn from a uniform distribution spanning values between 1.5 and 2.3. Results for ΔGSST and ΔGMST are shown in Fig. 2b and d.

Analysis of tropical Pacific cooling. As stated in the main text, we analyzed LGM cooling across the tropical Pacific in the proxy data alone, in order to compare with the data assimilation result. The proxy data were calibrated to SST as described in the previous subsection, and then the Pacific zonal gradient was computed for both the LGM and LH slices as the difference between the average SST in the western Pacific (10°S– 10°N, 130 – 170°E) and the eastern Pacific (5°S– 5°N, 75 – 140°W) region. We then computed the LGM − LH difference in the zonal gradient, yielding a median value of -0.2°C. These calculations were conducted for all 1,000 ensemble members, yielding an uncertainty of 1.0°C (2σ).

Climate sensitivity calculations. We calculate equilibrium climate sensitivity (ECS) as:

$$ECS = \frac{\Delta\text{GMST}}{\Delta R} \times F_{2\times CO2} \tag{7}$$

where ΔGMST is taken from the data assimilation, $F_{2\times CO2}$ is the forcing associated with the doubling of CO_2 from the preindustrial state, and ΔR is the total change in radiative forcing, including the slow feedbacks that affect the LGM climate state. In Figure 4, we present one solution that includes greenhouse gas and ice sheet forcing ($\Delta R = \Delta R_{GHG} + \Delta R_{ICE}$) and another that additionally includes aerosol forcing from mineral dust ($\Delta R = \Delta R_{GHG} + \Delta R_{ICE} + \Delta R_{AE}$). We estimate ΔR_{GHG} and $F_{2\times CO2}$ to be -2.81 ± 0.28 W/m^2 (90% CI) and 3.80 ± 0.38 W/m^2 (90% CI), respectively, using published equations [39]. These estimates assume a 90% CI uncertainty range of ± 10%, consistent with the assessment in successive IPCC reports [39]. ΔR_{ICE} accounts for the radiative forcing from surface albedo changes associated with the LGM ice sheets and exposed land due to lowered sea level. We calculate ΔR_{ICE} using an approximate partial radiative perturbation method [64] in CESM and also make use of additional published results in 11 PMIP2 and 3 models [4,65]. The resulting ΔR_{ICE} has a multi-model ensemble mean of -3.66 W/m^2 and a range from -2.59 to -5.20 W/m^2 (Extended Data Table 3). ΔR_{AE} was obtained from a published compilation of the top of atmosphere instantaneous direct radiative forcing of LGM dust in nine modeling studies [40]. ΔR_{AE} has a large spread, ranging from 0 to -2 W/m^2.

We also calculate a third solution for ECS that assumes a lower ice sheet efficacy (ε) [42], in which ΔR_{ICE} is multiplied by 0.65. This value of ε comes from assuming an average fractional influence of the ice sheet (ω) of 0.46 (taken from ref. [41]). We then use Eq. 11 in ref. [42] to calculate the corresponding ε, based on the mean values of ΔR_{GHG} and ΔR_{ICE} given above.

To propagate uncertainties into the final calculations of ECS, we used a Monte Carlo approach, sampling the full 1000-member posterior ensemble of ΔGMST, and combining these with 10,000 samples of each distribution of ΔR as well as $F_{2\times CO2}$. ΔR_{GHG} and $F_{2\times CO2}$ were assumed to be Normal distributions, while ΔR_{ICE} and ΔR_{AE} were treated as empirical random distributions because the limited number of samples (derived from modeling experiments) prevents us from knowing the shape of these distributions.

Code availability. The data assimilation method used in this paper is publicly available as the Matlab code package `DASH` on GitHub: `https://github.com/JonKing93/DASH`. The Bayesian forward models, `BAYSPAR`, `BAYSPLINE`, `BAYFOX`, and `BAYMAG` are likewise publicly available on GitHub from J. Tierney's homepage: `https://github.com/jesstierney`.

References

1. CLIMAP Project Members. The Surface of the Ice-Age Earth. *Science* 1131–1137 (1976).

2. Joussaume, S. & Taylor, K. Status of the paleoclimate modeling intercomparison project (PMIP). *World Meteorological Organization-Publications-WMO TD* 425–430 (1995).

3. MARGO Project Members *et al.* Constraints on the magnitude and patterns of ocean cooling at the Last Glacial Maximum. *Nature Geoscience* **2**, 127–132 (2009).

4. Braconnot, P. *et al.* Evaluation of climate models using palaeoclimatic data. *Nature Climate Change* **2**, 417–424 (2012).

5. Schmittner, A. *et al.* Climate sensitivity estimated from temperature reconstructions of the Last Glacial Maximum. *Science* **334**, 1385–1388 (2011).

6. Mix, A. C., Morey, A. E., Pisias, N. G. & Hostetler, S. W. Foraminiferal faunal estimates of paleotemperature: Circumventing the no-analog problem yields cool ice age tropics. *Paleoceanography* **14**, 350–359 (1999).

7. Crowley, T. CLIMAP SSTs re-revisited. *Climate Dynamics* **16**, 241–255 (2000).

8. Ballantyne, A., Lavine, M., Crowley, T., Liu, J. & Baker, P. Meta-analysis of tropical surface temperatures during the Last Glacial Maximum. *Geophysical Research Letters* **32** (2005).

9. Telford, R., Li, C. & Kucera, M. Mismatch between the depth habitat of planktonic foraminifera and the calibration depth of SST transfer functions may bias reconstructions. *Climate of the Past* **9**, 859–870 (2013).

10. Tierney, J. E. & Tingley, M. P. BAYSPLINE: A new calibration for the alkenone paleothermometer. *Paleoceanography and Paleoclimatology* **33**, 281–301 (2018).

11. Tierney, J. E., Malevich, S. B., Gray, W., Vetter, L. & Thirumalai, K. Bayesian calibration of the Mg/Ca paleothermometer in planktic foraminifera. *Paleoceanography and Paleoclimatology* (2019).

12. Snyder, C. W. Evolution of global temperature over the past two million years. *Nature* **538**, 226–228 (2016).

13. Schneider von Deimling, T., Ganopolski, A., Held, H. & Rahmstorf, S. How cold was the last glacial maximum? *Geophysical Research Letters* **33** (2006).

14. Holden, P. B., Edwards, N., Oliver, K., Lenton, T. & Wilkinson, R. A probabilistic calibration of climate sensitivity and terrestrial carbon change in GENIE-1. *Climate Dynamics* **35**, 785–806 (2010).

15. Shakun, J. D. *et al.* Global warming preceded by increasing carbon dioxide concentrations during the last deglaciation. *Nature* **484**, 49–54 (2012).

16. Annan, J. & Hargreaves, J. C. A new global reconstruction of temperature changes at the Last Glacial Maximum. *Climate of the Past* **9**, 367–376 (2013).

17. Bereiter, B., Shackleton, S., Baggenstos, D., Kawamura, K. & Severinghaus, J. Mean global ocean temperatures during the last glacial transition. *Nature* **553**, 39–44 (2018).

18. Friedrich, T. & Timmermann, A. Using Late Pleistocene sea surface temperature reconstructions to constrain future greenhouse warming. *Earth and Planetary Science Letters* (2019).

19. Masson-Delmotte, V. *et al.* Information from paleoclimate archives. In *Climate Change 2013: The Physical Science Basis. Contribution of Working Group I to the Fifth Assessment Report of the Intergovernmental Panel on Climate Change* (Cambridge University Press, Cambridge, 2013).

20. Brady, E. *et al.* The connected isotopic water cycle in the Community Earth System Model Version 1. *Journal of Advances in Modeling Earth Systems* **11**, 2547–2566 (2019).

21. Tierney, J. E. & Tingley, M. P. A Bayesian, spatially-varying calibration model for the TEX_{86} proxy. *Geochimica et Cosmochimica Acta* **127**, 83–106 (2014).

22. Malevich, S. B., Vetter, L. & Tierney, J. E. Global Core Top Calibration of $\delta^{18}O$ in Planktic Foraminifera to Sea Surface Temperature. *Paleoceanography and Paleoclimatology* **34**, 1292–1315 (2019).

23. Tardif, R. *et al.* Last millennium reanalysis with an expanded proxy database and seasonal proxy modeling. *Climate of the Past* **15**, 1251–1273 (2019).

24. DiNezio, P. N. *et al.* Glacial changes in tropical climate amplified by the Indian Ocean. *Science Advances* **4**, eaat9658 (2018).

25. Ford, H. L., Ravelo, A. C. & Polissar, P. J. Reduced El Niño–Southern Oscillation during the Last Glacial Maximum. *Science* **347**, 255–258 (2015).

26. Glushkova, O. Y. Geomorphological correlation of Late Pleistocene glacial complexes of Western and Eastern Beringia. *Quaternary Science Reviews* **20**, 405–417 (2001).

27. Bartlein, P. J. *et al.* Pollen-based continental climate reconstructions at 6 and 21 ka: a global synthesis. *Climate Dynamics* **37**, 775–802 (2011).

28. Roe, G. H. & Lindzen, R. S. The mutual interaction between continental-scale ice sheets and atmospheric stationary waves. *Journal of Climate* **14**, 1450–1465 (2001).

29. Löfverström, M. & Liakka, J. On the limited ice intrusion in Alaska at the LGM. *Geophysical Research Letters* **43**, 11–030 (2016).

30. Hopcroft, P. O. & Valdes, P. J. How well do simulated last glacial maximum tropical temperatures constrain equilibrium climate sensitivity? *Geophysical Research Letters* **42**, 5533–5539 (2015).

31. Porter, S. C. Snowline depression in the tropics during the Last Glaciation. *Quaternary science reviews* **20**, 1067–1091 (2000).

32. Stute, M. *et al.* Cooling of tropical Brazil (5°C) during the last glacial maximum. *Science* **269**, 379–383 (1995).

33. Lea, D. W., Pak, D. K. & Spero, H. J. Climate impact of late Quaternary equatorial Pacific sea surface temperature variations. *Science* **289**, 1719–1724 (2000).

34. Masson-Delmotte, V. *et al.* EPICA Dome C record of glacial and interglacial intensities. *Quaternary Science Reviews* **29**, 113–128 (2010).

35. Lee, J.-E., Fung, I., DePaolo, D. J. & Otto-Bliesner, B. Water isotopes during the Last Glacial Maximum: New general circulation model calculations. *Journal of Geophysical Research: Atmospheres* **113** (2008).

36. Rohling, E. J. *et al.* Making sense of palaeoclimate sensitivity. *Nature* **491**, 683–691 (2012).

37. Prentice, I. C., Jolly, D. & Biome 6000 Participants. Mid-Holocene and glacial-maximum vegetation geography of the northern continents and Africa. *Journal of Biogeography* **27**, 507–519 (2000).

38. Köhler, P. *et al.* What caused Earth's temperature variations during the last 800,000 years? Data-based evidence on radiative forcing and constraints on climate sensitivity. *Quaternary Science Reviews* **29**, 129–145 (2010).

39. Etminan, M., Myhre, G., Highwood, E. & Shine, K. Radiative forcing of carbon dioxide, methane, and nitrous oxide: A significant revision of the methane radiative forcing. *Geophysical Research Letters* **43**, 12–614 (2016).

40. Albani, S. *et al.* Aerosol-climate interactions during the Last Glacial Maximum. *Current Climate Change Reports* **4**, 99–114 (2018).

41. Shakun, J. D. Modest global-scale cooling despite extensive early Pleistocene ice sheets. *Quaternary Science Reviews* **165**, 25–30 (2017).

42. Stap, L., Köhler, P. & Lohmann, G. Including the efficacy of land ice changes in deriving climate sensitivity from paleodata. *Earth System Dynamics* **10**, 333–345 (2019).

43. Charney, J. G. *et al.* *Carbon dioxide and climate: a scientific assessment* (National Academy of Sciences, Washington, DC, 1979).

44. Knutti, R. & Hegerl, G. C. The equilibrium sensitivity of the Earth's temperature to radiation changes. *Nature Geoscience* **1**, 735 (2008).

45. Friedrich, T., Timmermann, A., Tigchelaar, M., Timm, O. E. & Ganopolski, A. Nonlinear climate sensitivity and its implications for future greenhouse warming. *Science Advances* **2**, e1501923 (2016).

46. Zhu, J., Poulsen, C. J. & Tierney, J. E. Simulation of Eocene extreme warmth and high climate sensitivity through cloud feedbacks. *Science Advances* **5**, eeax1874 (2019).

47. DiNezio, P. N. & Tierney, J. E. The effect of sea level on glacial Indo-Pacific climate. *Nature Geoscience* **6**, 485–491 (2013).

48. Chan, D., Kent, E. C., Berry, D. I. & Huybers, P. Correcting datasets leads to more homogeneous early-twentieth-century sea surface warming. *Nature* **571**, 393–397 (2019).

49. Hurrell, J. W. *et al.* The community earth system model: A framework for collaborative research. *Bulletin of the American Meteorological Society* **94**, 1339–1360 (2013).

50. Kageyama, M. *et al.* The PMIP4 contribution to CMIP6 – Part 4: Scientific objectives and experimental design of the PMIP4-CMIP6 Last Glacial Maximum experiments and PMIP4 sensitivity experiments. *Geoscientific Model Development* **10**, 4035–4055 (2017).

51. Peltier, W. R., Argus, D. F. & Drummond, R. Space geodesy constrains ice age terminal deglaciation: The global ICE-6G_C (VM5a) model. *Journal of Geophysical Research: Solid Earth* **120**, 450–487 (2015).

52. Zhu, J. *et al.* Reduced ENSO variability at the LGM revealed by an isotope-enabled Earth system model. *Geophysical Research Letters* **44**, 6984–6992 (2017).

53. Meehl, G. A. *et al.* Effects of Model Resolution, Physics, and Coupling on Southern Hemisphere Storm Tracks in CESM1.3. *Geophysical Research Letters* **46**, 12408–12416 (2019).

54. Hakim, G. J. *et al.* The last millennium climate reanalysis project: Framework and first results. *Journal of Geophysical Research: Atmospheres* **121**, 6745–6764 (2016).

55. Lauvset, S. K. *et al.* A new global interior ocean mapped climatology: the 1 × 1 GLODAP version 2. *Earth System Science Data* **8**, 325–340 (2016).

56. Gray, W. R. & Evans, D. Nonthermal influences on Mg/Ca in planktonic foraminifera: A review of culture studies and application to the last glacial maximum. *Paleoceanography and Paleoclimatology* **34**, 306–315 (2019).

57. Whitaker, J. S. & Hamill, T. M. Ensemble data assimilation without perturbed observations. *Monthly Weather Review* **130**, 1913–1924 (2002).

58. Houtekamer, P. L. & Mitchell, H. L. A sequential ensemble Kalman filter for atmospheric data assimilation. *Monthly Weather Review* **129**, 123–137 (2001).

59. Nash, J. E. & Sutcliffe, J. V. River flow forecasting through conceptual models part ia discussion of principles. *Journal of Hydrology* **10**, 282–290 (1970).

60. Werner, M. *et al.* Glacial-interglacial changes of H218O, HDO and deuterium excess-results from the fully coupled Earth System Model ECHAM5/MPI-OM. *Geoscientific Model Development Discussions* **9**, 647–670 (2016).

61. Atsawawaranunt, K. *et al.* The SISAL database: a global resource to document oxygen and carbon isotope records from speleothems. *Earth System Science Data* **10**, 1687–1713 (2018).

62. Comas-Bru, L. *et al.* Evaluating model outputs using integrated global speleothem records of climate change since the last glacial. *Climate of the Past* **15**, 1557–1579 (2019).

63. Gaspari, G. & Cohn, S. E. Construction of correlation functions in two and three dimensions. *Quarterly Journal of the Royal Meteorological Society* **125**, 723–757 (1999).

64. Taylor, K. *et al.* Estimating shortwave radiative forcing and response in climate models. *Journal of Climate* **20**, 2530–2543 (2007).

65. Braconnot, P. & Kageyama, M. Shortwave forcing and feedbacks in last glacial maximum and mid-holocene pmip3 simulations. *Philosophical Transactions of the Royal Society A: Mathematical, Physical and Engineering Sciences* **373**, 20140424 (2015).

Acknowledgements We thank Mathew Fox and Natasha Rapp for assistance with compiling the proxy SST data. This research was supported by National Science Foundation grant numbers AGS-1602301 and AGS-1602223, and Heising-Simons Foundation grant number 2016-015.

Author contributions JET designed the study, conducted the data assimilation, analyzed the results, and led the writing of this paper. JET and SBM compiled and quality-checked the proxy

SST data. SBM designed the proxy database and adapted BACON age modeling software to Python. JK wrote the DASH code used for the data assimilation, based on methods developed by GH. JZ and CP planned and conducted the iCESM simulations. All authors contributed to the writing of this manuscript.

Competing Interests The authors declare that they have no competing financial interests.

Data availability The LGM and Late Holocene proxy data are available as `.csv` format files (including both raw proxy values and calibrated estimates of SST). We also provide a gridded $5° \times 5°$ map of LGM $-$ LH proxy anomalies in `.netcdf` format. The posterior fields of the data assimilation product (SST, SSS, δ^{18}O of seawater, and $\delta^{18}O_p$ are available in `.netcdf` format. Files are available for download from Pangaea.de: [insert link when ready].

Correspondence Correspondence should be addressed to JET (email: jesst@arizona.edu).

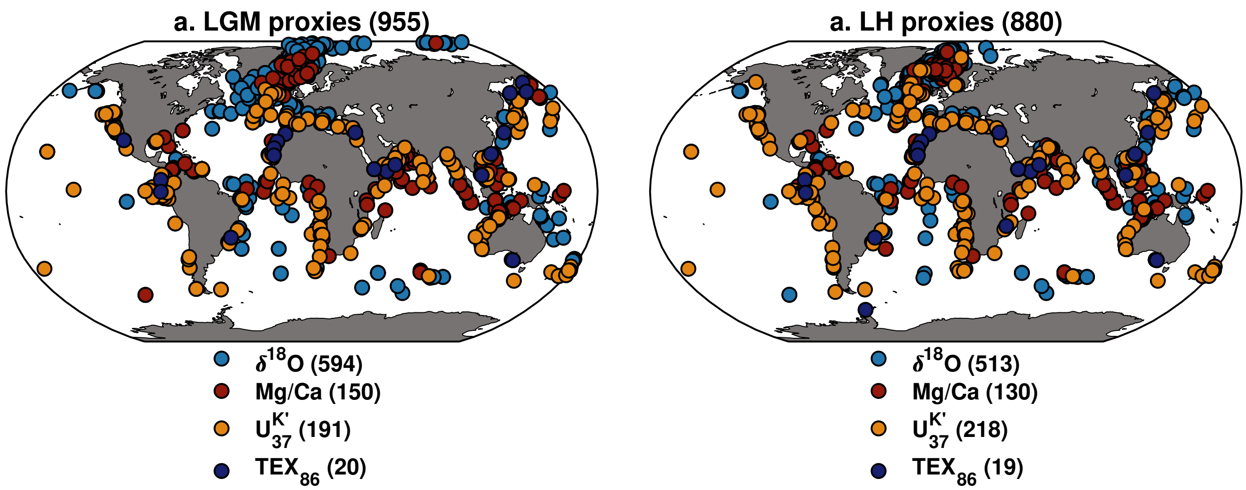

Figure 1: **Locations of geochemical sea-surface temperature (SST) proxies used for Last Glacial Maximum climate reconstruction.** a. Proxy sites for the LGM; b. Proxy sites for the Late Holocene (LH). Proxies are color-coded by type; the number of proxies is shown in parentheses.

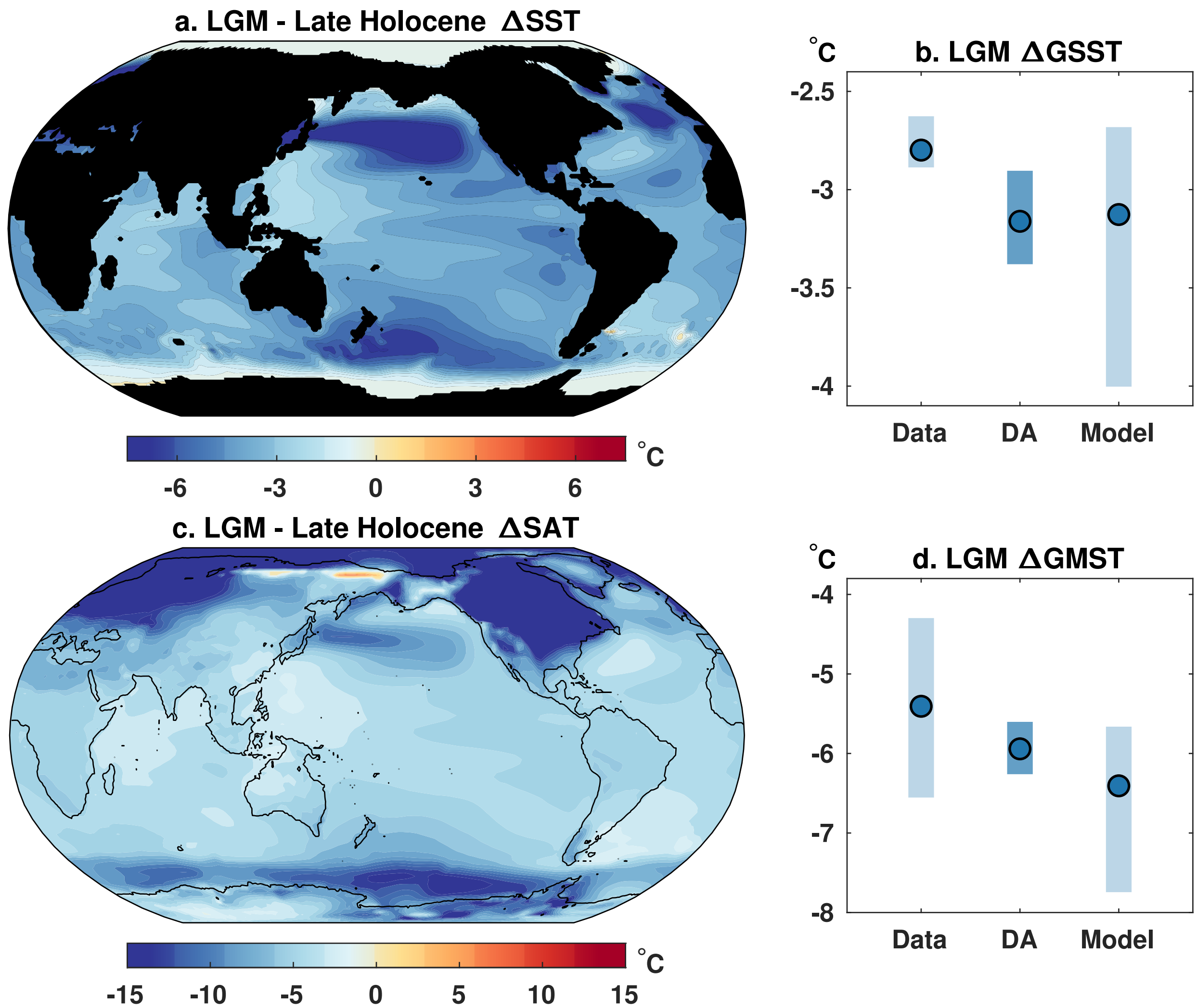

Figure 2: **Global changes in temperature during the LGM, derived from paleoclimate data assimilation** a. LGM - Late Holocene changes in sea-surface temperature (ΔSST); b. LGM - Late Holocene changes in surface air temperature (ΔSAT). c. LGM global mean sea-surface temperature change (ΔGSST) and d. LGM global mean surface temperature change (ΔGMST) derived from the data, the data assimilation (DA), and the model prior. Dots represent median values; bars show the 95% CI.

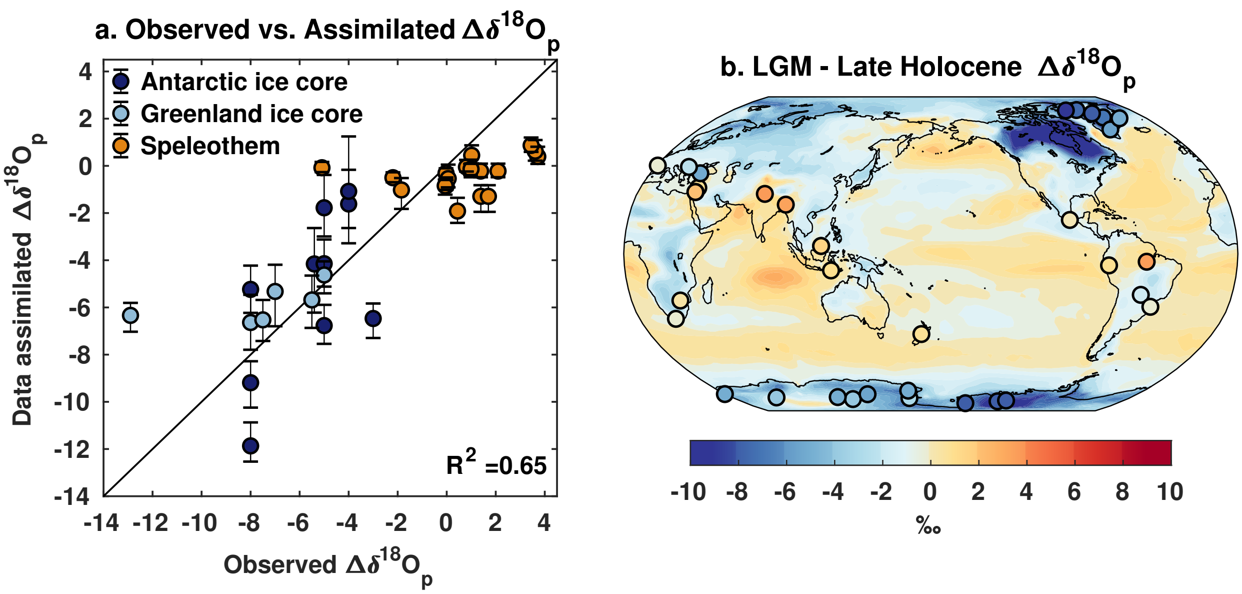

Figure 3: **Validation of the data assimilation with δ^{18}O of precipitation.** a. Observed changes in ice core and speleothem-inferred $\delta^{18}O_p$ compared to predicted changes from the posterior data assimilation ensemble. Dots indicate median values, error bars represent the 95% CI. R^2 value is shown in the lower right corner. b. Spatial map of median changes in the δ^{18}O of precipitation from the posterior ensemble, overlain with ice core and speleothem observations (dots). Speleothem δ^{18}O has been converted from δ^{18}O of calcite or aragonite to $\delta^{18}O_p$ (in ‰ VSMOW) prior to plotting (see Methods).

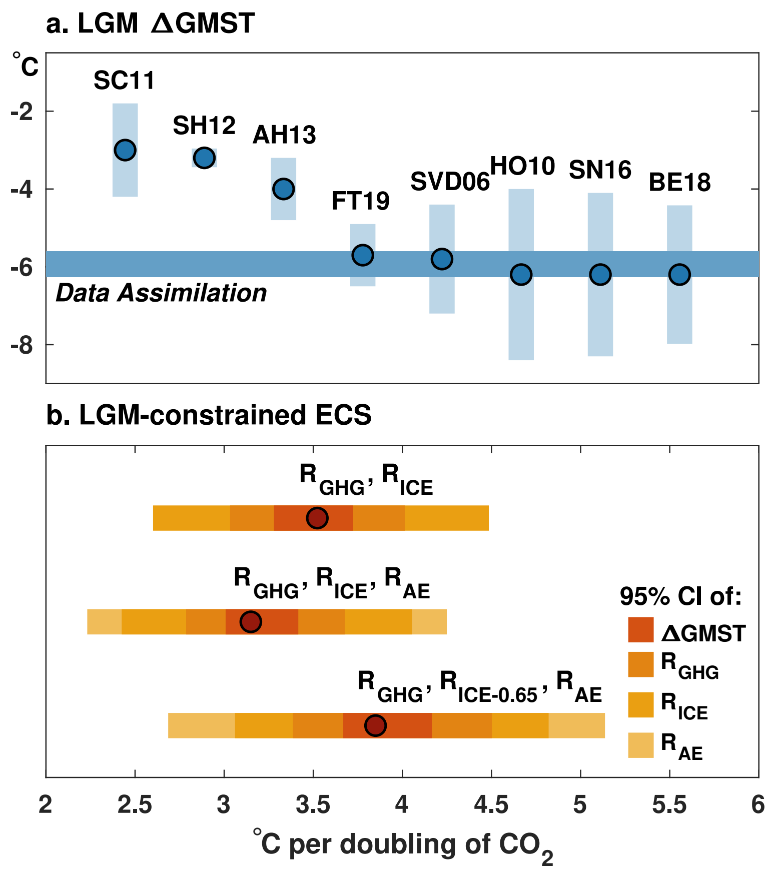

Figure 4: **LGM global temperature change and climate sensitivity derived from data assimilation.** a. Estimates of the change in global mean surface temperature (ΔGMST) from previous studies (vertical bars represent the 95% CI, dots show the median) compared to the data assimilation result (height of the horizontal bar represents the 95% CI). SC11 = ref. [5], SH12 = ref. [15], AH13 = ref. [16], FT19 = ref. [18], SVD06 = ref. [13], HO10 = ref. [14], SN16 = ref. [12], BE18 = ref. [17]. b. LGM-constrained equilibrium climate sensitivity (ECS), using the ΔGMST from data assimilation. Dots indicate median values. The red–yellow bars indicate the 95% CI associated with ΔGMST and radiative forcing estimates of greenhouse gases (R_{GHG}), ice sheets (R_{ICE}), and mineral dust aerosols (R_{AE}), respectively. The lower bar shows the distribution of ECS with an ice sheet efficacy of 0.65.

Extended Data Table 1. Validation statistics associated with scaling the global estimate of the proxy variance $\boldsymbol{R}_g$. CE and RMSE are calculated on the 25% of the proxy data withheld from the assimilation. R^2 is calculated between observed $\Delta\delta^{18}O_p$, from speleothems and ice cores, and data-assimilated $\Delta\delta^{18}O_p$ at the same locations. Localization was held constant at 12,000 km. "Prior" denotes comparison with the mean of the prior model ensemble.

	Prior	$\boldsymbol{R}_g$	$\boldsymbol{R}_g/2$	$\boldsymbol{R}_g/5$	$\boldsymbol{R}_g/10$	$\boldsymbol{R}_g/20$	$\boldsymbol{R}_g/100$
— LGM —							
CE	0.83	0.91	0.91	0.93	0.93	0.94	0.94
RMSE	0.40	0.30	0.29	0.27	0.26	0.25	0.25
— Late Holocene —							
CE	0.92	0.95	0.96	0.96	0.96	0.96	0.96
RMSE	0.28	0.22	0.21	0.20	0.20	0.20	0.20
— LGM – LH vs. $\Delta\delta^{18}O_p$ —							
R^2	0.37	0.42	0.52	0.63	0.66	0.66	0.44

Extended Data Table 2. Validation statistics associated with varying the cut-off radius of the covariance localization. CE and RMSE are calculated on the 25% of the proxy data withheld from the assimilation. R^2 is calculated between observed $\Delta\delta^{18}O_p$, from speleothems and ice cores, and data-assimilated $\Delta\delta^{18}O_p$ at the same locations. Cut-off radii are given in units of km; ∞ denotes no localization. Proxy variance $\boldsymbol{R}$ is held at $\boldsymbol{R}_g/10$.

	∞	24,000	18,000	12,000	9,000	6,000
— LGM —						
CE	0.89	0.92	0.93	0.93	0.93	0.93
RMSE	0.33	0.28	0.27	0.26	0.26	0.26
— Late Holocene —						
CE	0.94	0.95	0.96	0.96	0.96	0.96
RMSE	0.24	0.21	0.21	0.20	0.20	0.20
— LGM - LH vs. $\Delta\delta^{18}O_p$ —						
R^2	0.42	0.62	0.66	0.66	0.66	0.52

Extended Data Table 3. Compilation of estimates of ΔR_{ICE} used for calculations of ECS.

Model	$\boldsymbol{\Delta R_{ICE}}$	**Reference**
CCSM4	−3.79	PMIP3[65]
IPSL-CM5A-LR	−4.90	PMIP3[65]
MIROC-ESM	−5.20	PMIP3[65]
MPI-ESM-P	−4.57	PMIP3[65]
MRI-CGCM3	−3.62	PMIP3[65]
CCSM3	−2.59	PMIP2[4]
CNRM	−2.66	PMIP2[4]
HadCM3M2	−3.23	PMIP2[4]
HadCM3M2 v	−3.41	PMIP2[4]
IPSL-CM4	−3.48	PMIP2[4]
MICRO3.2	−2.88	PMIP2[4]
CESM1.2	−3.63	This study
Mean	**−3.66**	
$\boldsymbol{1\sigma}$	**0.84**	

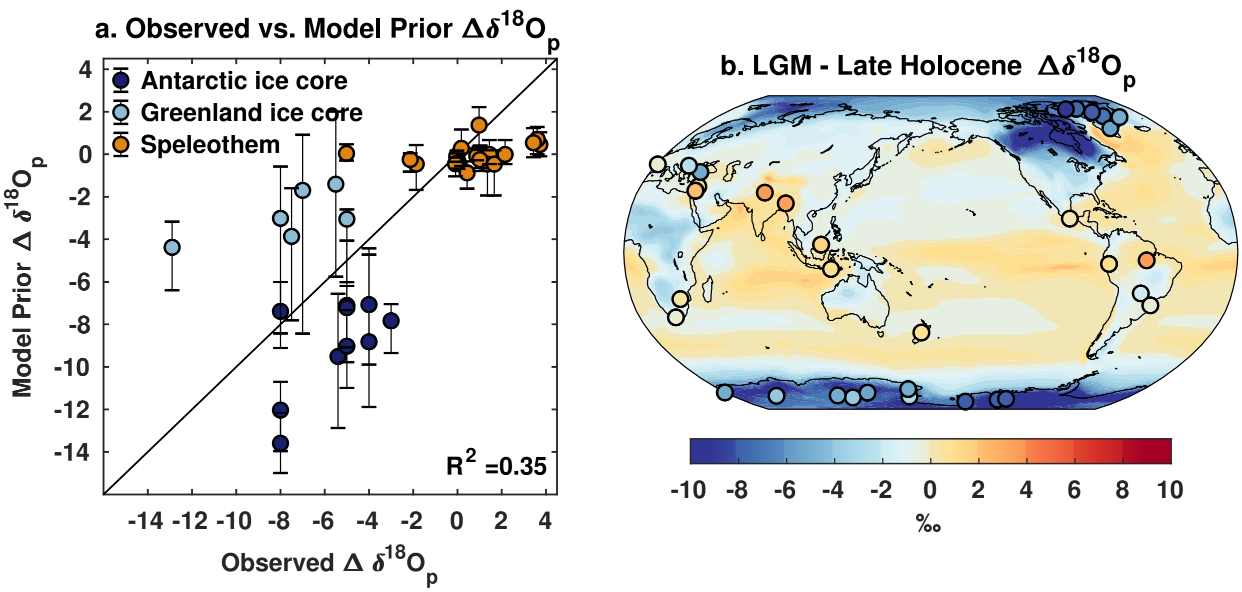

Extended Data Figure 1. Comparison of model prior $\delta^{18}O_p$ with speleothem and ice core proxies a. Observed changes in ice core and speleothem-inferred $\delta^{18}O_p$ compared to the model prior ensemble. R^2 value is shown in the lower right corner. b. Spatial map of median changes in the $\delta^{18}O$ of precipitation from the prior ensemble, overlain with ice core and speleothem observations (dots). Speleothem $\delta^{18}O$ has been converted from $\delta^{18}O$ of calcite or aragonite to $\delta^{18}O_p$ (in ‰ VSMOW) prior to plotting (see Methods).